CMOS optoelectronic spectrometer based on photonic integrated circuit for in vivo 3D optical coherence tomography

Anja Agneter[1†], Paul Muellner[2†], Quang Nguyen[1], Dana Seyringer[3], Elisabet A. Rank[1], Marko Vlaskovic[4], Jochen Kraft[4], Martin Sagmeister[4], Stefan Nevlacsil[2], Moritz Eggeling[2], Alejandro Maese-Novo[2], Yevhenii Morozov[5], Nicole Schmitner[5], Robin A. Kimmel[5], Ernst Bodenstorfer[2], Pietro Cipriano[4], Horst Zimmermann[6], Rainer A. Leitgeb[1], Rainer Hainberger[2] and Wolfgang Drexler[1*]

[†]Anja Agneter and Paul Muellner contributed equally to this work.

*Correspondence:
wolfgang.drexler@meduniwien.ac.at

[1] Center for Medical Physics and Biomedical Engineering, Medical University of Vienna, Waehringer Guertel 18-20/4 L, Vienna 1090, Austria
[2] AIT Austrian Institute of Technology GmbH, Gieffinggasse 4, Vienna 1210, Austria
[3] Research Centre for Microtechnology, Vorarlberg University of Applied Sciences, Hochschulstrasse 1, Dornbirn 6850, Vorarlberg, Austria
[4] ams OSRAM, Tobelbader Strasse 30, Premstaetten 8141, Styria, Austria
[5] Institute of Molecular Biology/CMBI, University of Innsbruck, Technikerstrasse 25, Innsbruck 6020, Tyrol, Austria
[6] Institute of Electrodynamics, Microwave and Circuit Engineering, TU Wien, Gußhausstraße 25/354, Vienna 1040, Vienna, Austria

Abstract

Photonic integrated circuits (PICs) represent a promising technology for the much-needed medical devices of today. Their primary advantage lies in their ability to integrate multiple functions onto a single chip, thereby reducing the complexity, size, maintenance requirements, and costs. When applied to optical coherence tomography (OCT), the leading tool for state-of-the-art ophthalmic diagnosis, PICs have the potential to increase accessibility, especially in scenarios, where size, weight, or costs are limiting factors. In this paper, we present a PIC-based CMOS-compatible spectrometer for spectral domain OCT with an unprecedented level of integration. To achieve this, we co-integrated a 512-channel arrayed waveguide grating with electronics. We successfully addressed the challenge of establishing a connection from the optical waveguides to the photodiodes monolithically co-integrated on the chip with minimal losses achieving a coupling efficiency of 70%. With this fully integrated PIC-based spectrometer interfaced to a spectral domain OCT system, we reached a sensitivity of 92dB at an imaging speed of 55kHz, with a 6dB signal roll-off occurring at 2mm. We successfully applied this innovative technology to obtain 3D in vivo tomograms of zebrafish larvae and human skin. This ground-breaking fully integrated spectrometer represents a significant step towards a miniaturised, cost-effective, and maintenance-free OCT system.

Keywords: Photonic integrated circuit, Optical coherence tomography, CMOS photonics, Optoelectronic, Integrated spectrometer, Electronic-photonic integration

Introduction

Photonic integrated circuits (PICs) enable building self-contained photonic systems by monolithically (co-)integrating various functional building blocks for guiding and manipulating light on a single chip [1]. PIC technology offers the potential of seamless integration with electronics by using complementary metal-oxide-semiconductor (CMOS) compatible materials as waveguide materials, such as silicon nitride [2].

Current semiconductor fabrication facilities can already produce PICs using standard processes. This ensures structural reproducibility and allows for efficient production of large quantities of chips in a single process flow, enabling scalable, high-precision, and cost-effective manufacturing. All these advantages make PIC technology a promising candidate to miniaturize medical diagnostic tools that employ optical measurement schemes and significantly reduce their production costs.

One such medical diagnostic tool is optical coherence tomography (OCT). In ophthalmology, OCT is the current gold standard imaging technique to diagnose retinal diseases [3]. Owing to its non-invasive, high-resolution 3D-imaging capability of relevant structures, OCT has become a useful imaging tool also in other medical disciplines, such as in dermatology [4, 5], cancer research [6, 7], and endoscopy [8]. However, the high cost and large footprint of current commercial OCT systems restrict OCT examinations to hospitals and large practices. Miniaturizing OCT and making it affordable are the two main contributors in increasing its availability for decentralized application and widespread screening - particularly in low resource settings such as the global south and in home-care [9, 10].

In previous studies aimed at miniaturizing OCT, tomograms were acquired using spectral domain (SD)-OCT systems that replaced single optical components such as interferometers [11], delay lines [12], or diffraction gratings [13–15] with PICs. A PIC-based analogue to a diffraction grating is an arrayed waveguide grating (AWG) [16–21]. It can be used in SD-OCT to separate broadband light into its different wavelengths. Such a system, where only the grating was replaced by a 256-channel AWG, already proved suitable for in vivo retinal imaging [22]. Important performance parameters for OCT, such as the axial resolution, the imaging depth, and the roll-off, are strongly influenced by the AWG. A wider bandwidth of the AWG is favorable for a better axial OCT resolution, while a small wavelength spacing between the channels enhances the imaging depth. To maximize both parameters, the number of channels must be as high as possible. In previous work [22], a CCD-camera and focusing optics that had to be precisely aligned with the AWG, were needed, limiting the reduction in size and ease of use. Integration with optoelectronic and electronic building blocks represents the next step towards a fully integrated OCT system on a chip.

However, monolithic integration of passive and active PIC components for the 800nm wavelength range has not yet been achieved. A prerequisite for the seamless integration of photodetectors is an efficient broadband coupling scheme to transfer light from the waveguide to the detector region. Methods such as micromirror- and microlenses-based vertical-coupling [23, 24], evanescent-coupling [25–27], and butt-coupling [28, 29], with PIC waveguides are commonly employed. However, these approaches have their limitations. Mirror couplers utilize an angled reflecting surface integrated into the waveguide plane to redirect light out of the waveguide towards a photodiode. These mirror interfaces entail complex fabrication processes. Evanescent-coupling schemes require photodetectors to be brought in close proximity to the waveguide, which is not always possible because of technological and chip design restrictions. Moreover, it needs a high alignment precision. Finally, butt-coupling also requires high alignment precision between waveguide and photodetector and involves complex regrowth processes for the photodetector materials. Another method relies on grating-assisted coupling, which so

far has been applied only in combination with photodiodes flip-chip bonded on top of PICs [30]. However, fabricating additional metal layers on the backside acting as mirrors is not possible in a CMOS-compatible way. Although amorphous silicon photodiodes are CMOS-compatible, their low responsivity, of only 0.03 A/W [31], is not suitable for highly sensitive imaging systems, such as OCT.

So far, electronic and optical components were only co-integrated by combining different materials supporting higher wavelength regions, which are neither CMOS-compatible nor suitable for ophthalmic OCT imaging [32, 33]. The main reason for this is the absence of a scheme that can couple light from waveguides to integrated photodiodes at low fabrication costs, while simultaneously meeting the high demands of applications such as OCT in terms of coupling efficiency. Furthermore, all approaches available so far have the disadvantage that with an increasing number of separate photodiodes/photodiode-arrays, the complexity and costs increase, too. In this paper, we introduce a novel grating and mirror coupler-based approach to efficiently transfer light from a waveguide to a PIN-photodiode that is monolithically co-integrated several micrometers beneath the waveguide (patent pending [34]). This approach is fully CMOS-compatible and can be incorporated into low-cost products, thereby, opening up new possibilities for OCT and other spectrometer based medical sensing concepts. Another advantage of the monolithic co-integration, is that the complexity and the fabrication costs remain the same regardless of the quantity of the photodiodes. Moreover, the positioning of the photodiodes is not limited to specific areas providing a maximum degree of design freedom. In addition to the photodiodes, also auxiliary electronic components (analogue front-end circuitry, analogue-to-digital converters (ADCs), and digital logic) are co-integrated on the chip to ensure high sensitivity in signal detection and low power consumption. The feasibility and implementation of these active components were reported in preparatory work [35, 36], which showed improved spectral responsivity for the silicon PIN-photodiodes.

We demonstrate the first PIC based 512-channel AWG, monolithically co-integrated with photodiodes, multiplexers, ADCs and control logic, all on a single chip for the 800 nm wavelength region. This chip is mounted on a printed circuit board (PCB) containing all the necessary electronics to function as line-scan detector. We provide a comprehensive performance characterization of the AWG and the novel coupling structure. We apply this fully integrated spectrometer to obtain three-dimensional in vivo OCT imaging of zebrafish larvae and human skin.

Results

Optoelectronic spectrometer

Figure 1 presents a photograph of the $2 \times 2\,\text{cm}^2$ spectrometer chip, which is wire-bonded to a printed circuit board (PCB). The PCB supplies power to the chip and connects it to a computer via a frame grabber. The silicon-based chip houses optical, optoelectronic, and electronic components serving as both a diffraction grating and a line-scan detector. The chip's size is primarily determined by the AWG. The main challenge lies in minimizing its footprint without comprising the AWG performance (detailed parameters are provided in the Methods section). The waveguides on the PIC, which guide light, consist of a silicon-nitride core and a silicon-dioxide cladding. The silicon-dioxide serves a dual
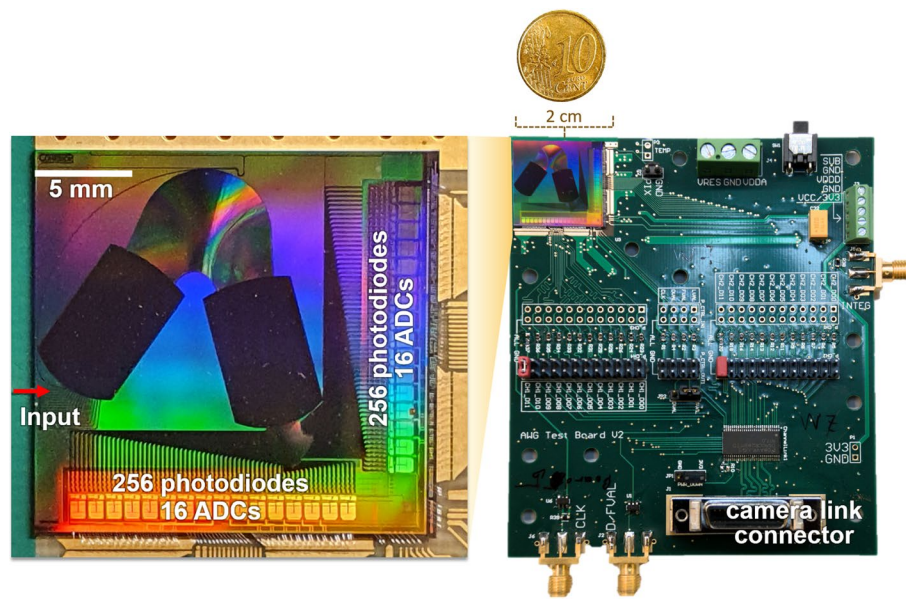
Fig. 1 Photograph of the PCB, including the PIC with co-integrated AWG, photodiodes and auxiliary electronics: Left side: a 2 × 2 cm^2 PIC with AWG, 512 photodiodes, and 32 ADCs (both on the south and the east side of the chip), Right side: the PIC is wire-bonded to the PCB, featuring a camera link connector for signal transmission to the computer via a frame grabber. Three SMA connectors are on the side of the PCB: Two of them are connected to external signal generators, providing a signal for the clock for the ADCs and the exposure control for the photodiodes. The third connector is used to send a trigger signal from the PCB to the frame grabber

purpose, forming part of the waveguide structure and separating the waveguide from the optoelectronic substrate that would otherwise absorb the light.

To minimize the in-coupling losses into the AWG, we designed an inverted taper and measured average losses of 1.9 dB in the wavelength range of 850 − 900 nm, using glycerol as index-matching fluid between fiber and the chip edge. In the 850 − 900 nm wavelength range we determined propagation losses of 1.56 dB/cm. The length of the waveguide depends on the position of the photodiode on the chip, ranging from 5 mm to 15 mm.

Figure 2a depicts a detailed illustration of the AWG design, along with its co-integrated electronics. To characterize the AWG, we performed a wavelength scan from 856.52 nm to 904.23 nm, as shown in Fig. 3a. Zooming into individual channels, one can observe the spectral behavior and the crosstalk between the channels. We measured an average channel spacing of 0.093 nm. The maximum difference in the peak heights between the outer and the central channels is 5.2 dB, referred to as AWG insertion loss uniformity (ILU). This high ILU is mainly attributed to the size constraints of the chip.

The spectral behavior repeats across multiple diffraction orders, making the AWG suitable for different wavelength regimes. Each wavelength can be assigned to a pixel resulting in a linear wavelength-to-pixel mapping, as seen in Fig. 3b. This mapping also reveals the bandwidth of each order, which is 44 nm for the first and 47.71 nm for the second order. Additionally, it shows the wavelength spacing, which slightly increases from 5.3 nm to 10 nm between the first and second orders and between the second and third orders.
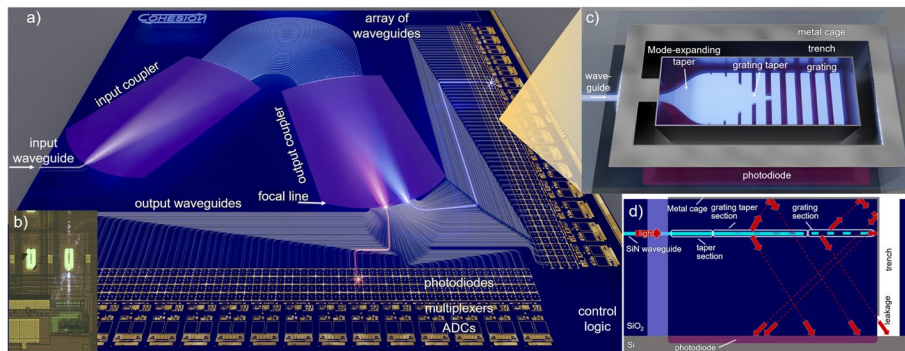
Fig. 2 Optoelectronic PIC based AWG: **a** Illustration of a PIC with an AWG co-integrated with active-pixel sensors (3T-PIN-photodiodes, amplifiers), multiplexers, ADCs and control logic. Light is coupled into the input waveguide and is then distributed across the entire array of waveguides through the input coupler. Due to the different path lengths of the waveguides in the phased array, the light propagating through these waveguides experiences different phase delays. These phase delays depend on the wavelength. Consequently, each wavelength constructively interferes at a different position of the focal line in the output coupler. Waveguides located along the focal line collect specific wavelengths and guide them to the corresponding photodiodes. The signals of 16 photodiodes are each buffered and digitized by an ADC. **b** Optical microscope image of an individually addressed waveguide-to-photodiode coupling structure. **c** Illustration of the waveguide-to-photodiode coupling structure: Light is coupled into the grating via a mode-expanding taper allowing a small footprint and a grating taper reducing back-reflections into the waveguide. An aperiodic grating deflects the light down to the photodiode. The entire structure is enclosed with a trench and a metal cage maximizing broadband efficiency and minimizing crosstalk to neighboring photodiodes (the top metal layer was omitted in the Figure). **d** Cross-section of the coupling structure (shown in **c**). The red arrows indicate the light paths beginning from the waveguide entering the coupling structure on the left. Light is reflected at the metal cage and coupled to the photodiode at the bottom
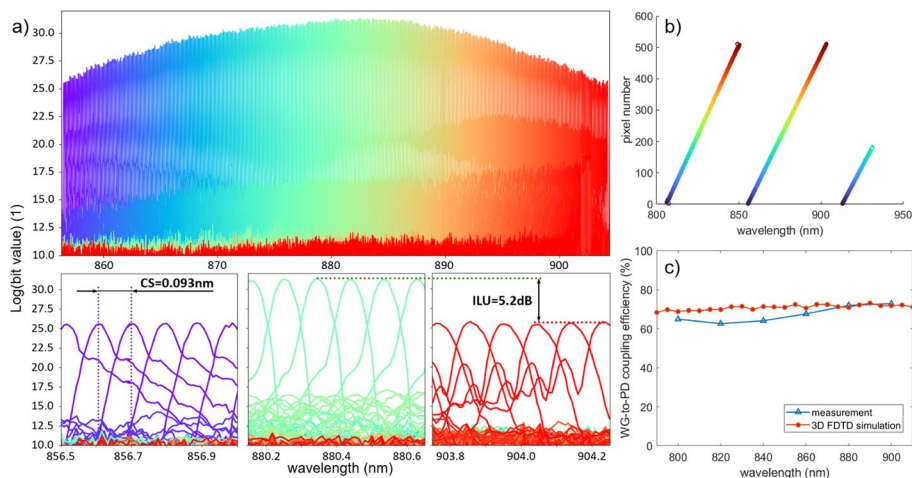

Fig. 3 Measurements of optoelectronic PIC based AWG: **a** Transmission spectrum in logarithmic scale acquired by scanning a tunable laser source through the wavelength range of 856.52 — 904.23 nm. Each color corresponds to the signal of one photodiode. At the bottom: zoomed in on the first (shortest wavelength), central, and last (longest wavelength) six channels. *CS*: channel spacing, *ILU*: AWG insertion loss uniformity. **b** Wavelength-to-pixel mapping in the wavelength range from 806 — 931 nm, showing multiple spectral orders of the AWG with wavelength gaps of 5.3 nm and 10 nm between them. **c** Measurement and 3D Finite-Difference Time-Domain (FDTD) simulation of the coupling efficiency of the light from the waveguide to the photodiode

Figure 2c and d provide a schematic representation of the new waveguide-to-photodiode coupling structure. This structure is designed to achieve broadband, low-loss coupling of light from the waveguide layer to the photodiode beneath, while maintaining CMOS compatibility. This requires a vertical transfer of light from the waveguide through the silicon dioxide lower cladding layer to the photodiode. The incident light propagating through the waveguide is efficiently coupled into an aperiodic grating structure via a tapered coupling mechanism (detailed parameters are provided in the Methods section).

The aperiodic nature of the grating ensures minimal back-coupling of the reflected light into the waveguide. The integrated taper includes a mode-expanding section, which widens the mode field to match the width of the photodiode, and a taper within the grating to minimize reflections back into the waveguide. A metal cage defines a confined optical environment. Within this confined space, the light undergoes multiple reflections from the metal walls, which redirects the light towards the photodiode. Thereby, the efficiency of light collection and spatial localization of the optical signal for subsequent detection and analysis is optimized.

We conducted 3D-FDTD simulations (see PIC design and fabrication section and measurements of the coupling efficiency from 800 nm to 900 nm, shown in Fig. 3c. For our new coupling structure, an efficiency of more than 70% is measured in the higher wavelength range, which is in good agreement with the simulation results. The losses primarily result from light passing through gaps between the metal cage and the photodiode, which we also confirmed in our simulations (see video in the extended data). This is supported by the bright-field micrograph displayed in Fig. 2b. Our simulations indicate that extending the metal cage further down to the photodiode could prevent almost all losses. In addition, we measured a maximum variation of only 5% throughout the entire wavelength range, affirming the suitability of this coupling scheme for broadband applications. Especially for OCT, a maximum coupling efficiency over a spectral range of 50 nm and beyond is required.

The analogue signal of the photodiodes is buffered, multiplexed, and directly converted to digital format on the chip using 32 integrated ADCs, as depicted in Fig. 2a. In detail, the output signals of 16 pixels are multiplexed to one successive approximation switched capacitor 12-bit (SAR) ADC with a sampling rate of 1.5 MS/s. The SAR ADC architecture was chosen due to its low power consumption and small footprint. So, the overall chip power consumption is only 800 mW [36]. The outputs of the 32 ADCs are multiplexed to two 12-bit output busses, which are accompanied by camera link protocol signals generated by the control logic block. The chip constitutes a fully integrated active pixel sensor employing 3-transistor (3T) PIN-photodiode pixels with in-pixel correlated double sampling allowing global shutter operation. Detailed descriptions of the photodiodes optimized for a high signal-to-noise ratio (SNR) can be found in [35].

This chip is wire-bonded to a PCB that provides power, the clock signal, and the integration time signal for the photodiodes. The PCB also transports the digital signal from the chip to the computer via a camera link chip and a corresponding connector.

Two external signal generators provide the clock signal for the ADCs and control the exposure time for the photodiodes. This setup allows us to adjust the clock frequency and exposure time to optimize signal transmission and the integration time of the

photodiodes. After experiments, we determined that the optimal exposure time signal is a square wave with a frequency of 55 kHz and a 90% duty cycle, coupled with a clock rate of 28 MHz (with a 50% duty cycle). It is important to note that the exposure control also plays a role in regulating the data transfer rate in addition to influencing the integration time of the photodiodes. Higher data transfer rates are constrained by the capabilities of the ADCs, which are limited by the minimum time required for data transfer.

In vivo OCT measurements

To demonstrate the suitability of the fully integrated spectrometer for in vivo OCT, we constructed a fiber-based SD-OCT setup, replacing the conventional spectrometer with the presented chip. In this system, depicted in Fig. 4a, we achieved a maximum sensitivity of 92 dB with 2.6 mW on the sample, an axial resolution of 13 μm in soft tissue (n=1.4) and a lateral resolution of 11 μm (see Fig. 4b). The acquisition speed of one A-scan (A-scan rate) is determined by the exposure control of the photodiodes and set to 55 kHz (described in detail in Methods OCT setup and image acquisition section).

   SD-OCT systems suffer from signal roll-off with increasing imaging depth. In addition to limitations in spectral resolution and sampling with finite pixel size, standard
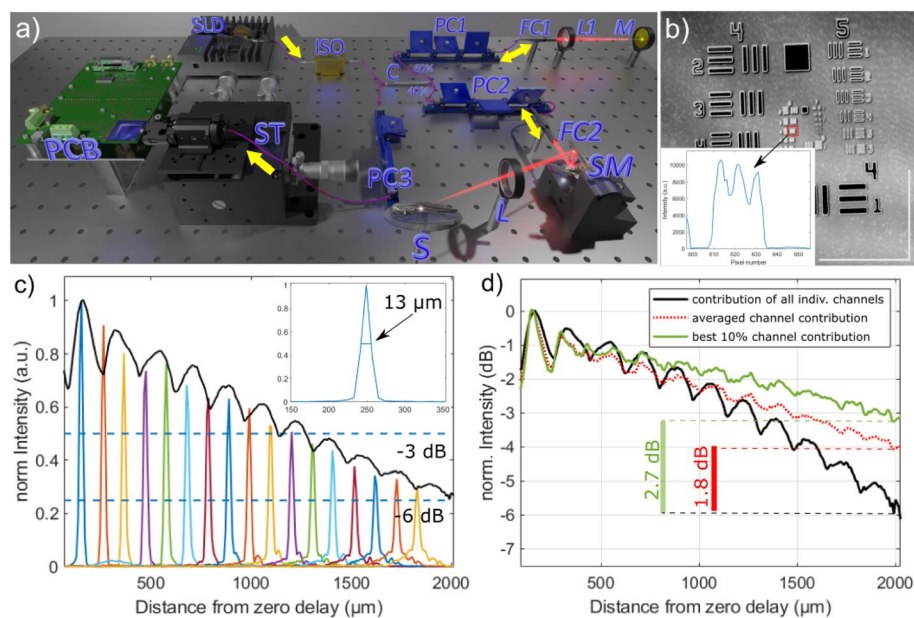

Fig. 4 Spectral domain(SD-)OCT setup with characteristic parameters and its signal roll-off: **a** 3D model of the OCT setup with the active PIC-based AWG as spectrometer. Key components include SLD: superluminescent diode, ISO: optical isolator, C: fiber splitter to split light into reference arm (60%) and sample arm (40%), PC: polarization controller, FC: fiber collimator, L: lens, M: mirror, SM: scan mirrors, S: sample, ST: 3-axis stage, PCB: printed circuit board. Yellow arrows indicate the direction of the light. **b** Maximum intensity projection of a resolution target. Inset: Reflection profile of group 6 element 4 giving a lateral resolution of 11 μm, white scale bars correspond to 0.5 mm. **c** Measurement of signal roll-off: A-scans with a mirror as sample at increasing distances from the zero delay (depths), dashed lines: indicates −3 dB (50%) and −6 dB (25%) of the signal. The signal decreases by 3 dB after 1.2 mm. Black curve indicates simulated envelope of roll-off. Inset: Point spread function (A-scan) indicating an axial resolution of 13 µm in tissue. **d** Simulated envelopes of the signal roll-off by using the spectral responses (Fig. 3a) from all individual channels (black curve), an averaged channel contribution (dotted, red curve) and only the best 10% of the channel responses (green curve). The signal decay could increase by 2.7 dB at 2 mm by reproducing the best channel responses across the entire AWG

SD-OCT systems with an external camera experience crosstalk between the photodiodes due to an imperfect alignment of the projection optics.

In our system, the crosstalk depends solely on the properties of the AWG, since each waveguide is directly coupled to one photodiode using the coupling structure described above. The roll-off envelope is calculated based on the spectral response functions of each AWG-channel (Fig. 3a). These calculations reproduce well the actual roll-off measurements, as depicted in Fig. 4c. We measured a 6 dB roll-off at 2 mm, which covers almost the entire imaging depth of 2.2 mm in air. Moreover, the calculations indicate that the behavior of the roll-off only depends on the spectral content of the AWG output waveguides. This finding is further supported by simulating a roll-off envelope by reproducing the response function of only the best 10% of the channels with the lowest roll-off across the entire AWG. This would improve the signal decay by 2.7 dB at 2 mm (seen in Fig. 4d).

With this PIC-based system, we can acquire in vivo tomograms that provide relevant morphological information in human fingertips and zebrafish larvae. Zebrafish are widely used as a model for human pathogenesis [37], including heart failure models [38] or cancer models [39, 40]. Figure 5a displays the 3D-tomogram of a whole zebrafish larva at an age of 4.5 days post fertilization (video in the extended data). When zooming into the upper part of the larva, morphological structures such as the eye, ear, spinal cord, swim bladder and the yolk sac are clearly visible in the en face projection (see Fig. 5b). While the heart is only faintly recognizable in this OCT tomogram, it becomes
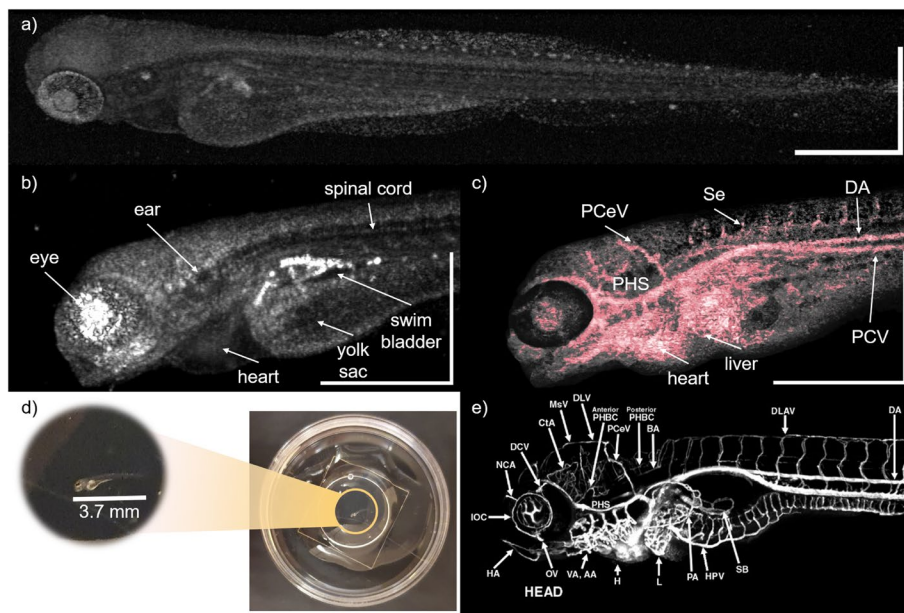

Fig. 5 In vivo OCT volume and OCTA of a zebrafish larva aged 4.5 days post fertilization obtained with our PIC-based, optoelectronic OCT-system **a** Volume of the zebrafish larva, five times averaged (rotating volume in Extended Data). **b** *En face* projection of the upper part of the zebrafish larva, averaged ten times. **c** OCTA maximum intensity projection of the zebrafish larva from b showing the heart (H), liver (L), and blood vessels, including: PCeV: posterior cerebral vein, PHS: primary head sinus, Se: intersegmental vessels, DA: dorsal aorta, all scale bars correspond to 0.5 mm. **d** Sample mounting for imaging the zebrafish: Anesthetized larva is embedded in Pythagel and placed into a glass-bottomed Petri dish. **e** Angiogram of zebrafish vessel anatomy from [42]

well contrasted in the OCT angiography (OCTA) in Fig. 5c. OCTA only requires additional processing steps (see Methods section) and by following these steps, the vascular system of the zebrafish larva becomes readily visible. The vessel pattern provides valuable insights into their growth and pathogenesis [41]. Apart from the heart, important vessels like the dorsal aorta, the posterior cerebral vein, the vasculature indicating the liver, and even small blood vessels in the eye can be distinguished. The vessels from the OCTA image can be easily identified by comparing them with the angiogram from literature [42], see Fig. 5e.

In addition, we obtained in vivo tomograms of human skin at the fingertip (glabrous skin), as depicted in Fig. 6. Benefiting from the low roll-off, the imaging capability extends from the epidermis down to the first layer of the dermis, despite the high absorption of light in tissue at the used wavelengths. Averaging over two or five B-scans makes the structural layers of the epidermis clearly distinguishable. Furthermore, the sweat ducts are easily visible and detectable even without the need for averaging. Beyond this, no additional structural insights can be obtained by averaging over 100 B-scans. For a detailed relation between the image SNR, contrast-to-noise ratio (CNR) and the number of averages, see Fig. 8 (in Characterization of OCT system section). This suggests that a limited number of B-scans are sufficient for the averaging process, consequently reducing the acquisition time. These tomograms are acquired with a B-scan rate of 45.8 Hz (1200 A-scans per B-scan), which corresponds to an acquisition time of 22 ms per B-scan.

Discussion

In this work, we successfully co-integrated an AWG, photodiodes, analogue front-end circuitry, and ADCs on a single CMOS-compatible PIC for the first time. The AWG features 512 channels covering a bandwidth of 47 nm while still maintaining a compact footprint of $2 \times 2\,cm^2$. With our novel coupling structure, we measured a coupling efficiency of 70% between the waveguide and the photodiode in the wavelength range
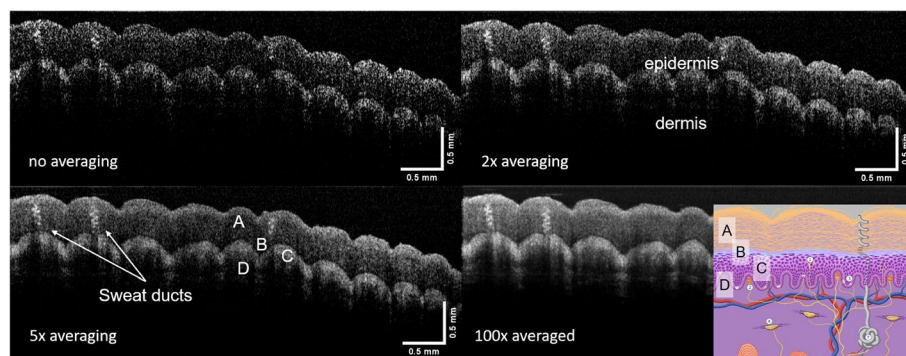

Fig. 6 In vivo tomograms obtained with our PIC-based, optoelectronic OCT-system of a human fingertip revealing the structure of the epidermis: No averaging, two times averaging, five times averaging, and 100 times averaging are demonstrated on the same fingertip region. For the relation between the image SNR and CNR and the number of averages, see also Fig. 8 The insert depicts a schematic drawing of glabrous skin (Illustration: www.hegasy.de [43] CC-BY-SA-4.0) illustrating the different layers of the epidermis: A: stratum corneum, B: stratum lucidum, C: stratum granulosum and stratum spinosum, D: stratum basale and stratum papillare

of 850 nm to 900 nm. By incorporating this chip into an SD-OCT system, we achieved a sensitivity of 92 dB and a 6 dB signal roll-off at 2 mm with an A-scan rate of 55 kHz. Our OCT tomograms of zebrafish larvae and human skin demonstrate its suitability for in vivo imaging, where relevant morphological structures can be distinguished with only two averages. Our system is capable of acquiring OCTA images, providing label-free insight into fine tissue vasculature.

The axial resolution, the imaging depth and the roll-off are important parameters for OCT. Improving them can be achieved by maximizing the number of AWG channels. This increases the bandwidth of the AWG and decreases the wavelength spacing between the channels, but, in turn, it also increase the AWG's footprint. Compared to the previous design [22], we doubled the number of AWG-channels and observed an improvement in imaging depth and roll-off. We suggest that the improved signal decay (see Fig. 4c) could be attributed to the absence of free-space projection optics. When the AWG spectrum was projected onto an external CCD-camera, the imperfect alignment of the projection optics caused additional crosstalk between the photodiodes, contributing to the signal roll-off.

Moreover, by integrating the photodiodes monolithically with the AWG on a single chip, our system becomes more robust and one step closer to a maintenance-free system. The integration is realised by our new CMOS-compatible, highly efficient waveguide-to-photodiode coupling structure. The high efficiency stems from the metal cage surrounding the whole coupling structure that prevents light from escaping the structure independently from the wavelength. The main contributors to the still remaining coupling losses are the gaps between the reflective metal cage and the photodiode as revealed in our simulations. Extending the metal cage down to the photodiode could prevent almost all losses. Unfortunately, due to current fabrication limitations this cannot be realized. In addition, the aperiodicity of the waveguide grating is important for the coupling efficiency. It prevents the coupling of back-reflected light from the top of the metal cage into the coupling structure.

The major challenges we encountered with the AWG are the losses and the quality of the spectral response (see Fig. 3a). We observed a more pronounced deviation of the spectral response between simulation and practical implementation compared to previous work [22] with less AWG-channels. As the number of AWG-channel is doubled and the footprint is restricted by the lithographic process, the AWG losses and crosstalk increase. AWG losses and crosstalk are mainly influenced by propagation losses, irregularities in the fabricated waveguide cross-section and design procedures. Moreover, the size limitations lead to a close placement of the waveguides in the phased array of the AWG, which increases the unwanted coupling between these waveguides contributing to the crosstalk. Therefore, we could enhance the AWG performance by increasing its footprint as well as by optimizing the design and fabrication process. Simulations of various AWG designs demonstrated how the AWG insertion losses (IL) or the adjacent channel crosstalk (AX) can be further optimized. The ILU can be improved by increasing the size of the AWG couplers, which would also improve the signal decay in depth. This decay is worsened by the stronger crosstalk of the outermost channels. In theory, lengthening the couplers could reduce the IL but due to limitations of the maximum field size in state-of-the-art projection lithography systems, this is not a viable option [44].

Optimizing channel crosstalk in the original AWG design would lead to an improvement of the AX by 7 dB with an AWG size of just $2.5 \times 2.5\,\text{cm}^2$, without affecting the AWG insertion losses [44]. With the proposed improvements of the spectral behavior of the AWG, the roll-off could even be lower than that of commercial SD-OCT systems. Increasing the imaging depth without increasing the number of channels, would be possible by employing additional signal processing steps, similar to full-range complex OCT [45, 46]. By also making use of the complex conjugate of the Fourier transform, the imaging range doubles, coming closer to commercially available spectrometers.

Although imaging speed is determined by camera specifications, our system, with integrated photodiodes and ADCs, is one of the fastest among previous AWG-based OCT systems. Implementing more than two digital 12-bit output busses and integrating a pipeline ADC [47], with a 25 MS/s sampling rate using $0.35\,\mu\text{m}$ CMOS can increase the A-scan rate by a factor of 16. However, this comes at the cost of higher power consumption and a larger chip area. Choosing a smaller feature size CMOS technology for the entire application-specific integrated circuit (ASIC) implementation will allow for even higher A-scan rates.

Our system represents a significant leap towards a fully integrated SD-OCT system on a chip. A potential reduction in the size and cost of the PCB is illustrated in Fig. 7 (right). The PCB can be down-sized by eliminating the test structures used for probing every data channel (bit) of the chip individually and using only a single connector for the power supply, clock signal, and exposure control. Replacing the camera link connection protocol with a USB controller and connector would not only reduce the size but also significantly cut costs. Additionally, employing a field programmable gate array (FPGA) to process the data directly on the PCB could enhance the processing speed and sensitivity. For further improvements, the design of the AWG could be adapted to be linear in frequency (k-space). Designing a conventional spectrometer to be linear in k-space
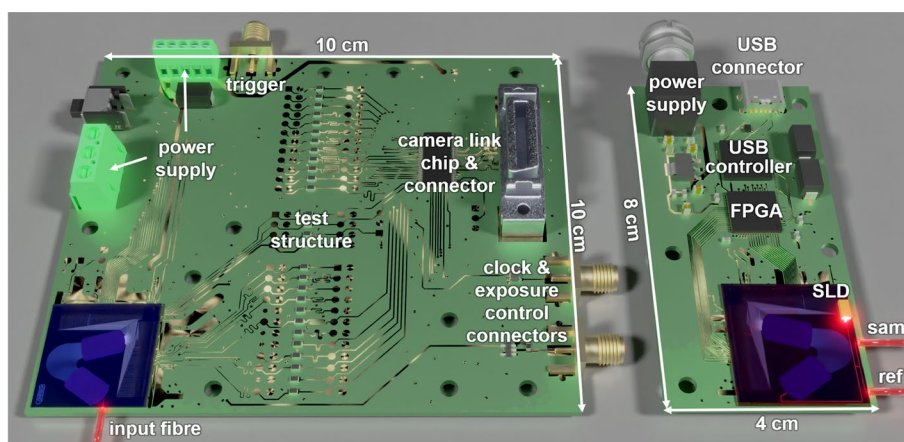

Fig. 7 Illustration of PCB: **Left**, Illustration of the current PCB ($10 \times 10\,\text{cm}^2$) described in this paper, demonstrating two connectors for the power supply, SMA connectors for the clock and exposure control, and one as a trigger output, a test structure to probe each data channel, as well as a camera link chip and connector. **Right**, Illustration of the proposed mock-up of the PCB ($4 \times 8\,\text{cm}^2$) with new electronics including a Field Programmable Gate Array (FPGA), a connector for power supply (LEMO), and USB controller and connector. Additional PIC components schematically illustrated: integrated SLD and integrated interferometer with two outputs to the sample arm (sam) and the reference arm (ref)

typically involves additional components such as prisms for redirecting the beam to the line-scan camera [48].

In an AWG, different wavelengths are focused along the focal line of the output coupler with a linear dependence between wavelength and the position at the focal line. In our work, the signal was sampled with linearly spaced output waveguides. By shifting the positions of the output waveguides using three different methods (the proportional method [21], angular method [49], and position method [50]) a channel spacing linear in k-space could be achieved in future designs. This modification would enable a fully integrated linear-in-k-spectrometer, with the potential to further improve the roll-off and also the axial OCT resolution. To enhance the robustness and compactness of the entire system, additional components such as an interferometer and an SLD could be integrated into the PIC. In such a setup, only two fibers for the sample and reference arms would need to be attached. To create a completely maintenance-free system, these fibers could be permanently attached or glued to the PIC.

Conclusion

Here, we present a significant advancement towards the realization of a fully integrated PIC-based OCT system on a chip. Our optoelectronic spectrometer, where we monolithically integrated optical and electronic components for the 800 nm wavelength region for the first time, proved suitable for in vivo OCT imaging. Moreover, it indicates that a direct translation to ophthalmology would be possible as retinal imaging is also performed in the same wavelength range. This integration is efficiently realized by our innovative coupling structure that minimizes the signal losses and is readily applicable for various chip designs without increasing the costs. While further improvements are needed to develop a small, robust and commercially viable SD-OCT system, our work has taken a significant step forward in developing a miniaturized, high-performance and cost-effective system for various applications.

Methods

AWG design

The design of the 512-channel AWG-spectrometer is based on the model by Smit and van Dam [18]. This model provides the necessary calculations for AWG dimensions, crucial for creating the AWG layout and conducting simulations using commercial photonics software tools. For comprehensive understanding of an AWG, you can refer to [19].

Given the strong correlation between the AWG structure's dimension and its performance, it is imperative to calculate the AWG design parameters with a high degree of precision. The width of the coupler is not a dominant parameter and can be adjusted as needed. The number of output waveguides (*Num*), for which the AWG is designed, equals 512 in our case. The number of arrayed waveguides, *Na*, is typically derived from the width of the far-field intensity divided by the minimum separation between arrayed waveguides, denoted as *dd*. This calculation ensures that all the light from the input star coupler is collected by the input array aperture [51]. For these calculations, we utilized the AWG-Parameters tool [18, 19], which has already been employed in numerous AWG designs, with successful experimental validation[20, 22, 51]. The AWG design

parameters for the 512-channel AWG-spectrometer were computed based on a central wavelength of $\lambda c = 850$ nm and a resolution of 0.1 nm (also referred to as channel spacing), corresponding to a frequency of $df = 42$ GHz. These parameters were determined as follows:

- minimum separation between PA waveguides, $dd = 2.3\,\mu$m,
- minimum separation between input/output waveguides, $dx = 3.5\,\mu$m,
- length of the star coupler $Lf = 8332.56\,\mu$m, and
- length-difference between adjacent waveguides in the phased array $\Delta L = 8.137\,\mu$m.

The final AWG structure was created and simulated in Optiwave's PHASAR tool [52] The performance parameters are defined as follows [19]:

- AWG Insertion loss (*IL*) of a channel is defined as the power loss measured from the smallest peak of the optical power of a channel within the entire spectrum to the 0-dB reference line.
- AWG Insertion loss uniformity (*ILU*), often referred to as non-uniformity (*Lu* [18]), is defined as the difference between the maximum and minimum AWG insertion losses across all output channels. It is consistently present and follows the far-field intensity in the output coupler as illustrated in Fig. 3a.
- Adjacent channel crosstalk (*AX*) can be characterized as the power induced by a selected channel in its neighboring channel, and vice versa. The worst-case value observed across all channels defines the adjacent channel crosstalk. A higher parameter value indicates better channel isolation, resulting in lower channel crosstalk.
- Background crosstalk (*BX*) is defined as the median peak of the optical power in the *BX*-band of the channel. The *BX*-band encompasses all wavelengths except those in the region of the channel center wavelength $\pm$ channel spacing. It represents the worst-case scenario across all channels. A higher parameter value indicates better channel isolation.

As the AWG is tailored to achieve specific performance criteria, the parameters *ILU* and *AX* are also used as the input parameters in the calculation of the AWG design parameters. In the case of the 512-channel AWG-spectrometer, the design aimed to achieve an AWG insertion loss uniformity of $ILU = 1.5$ dB and an adjacent channel crosstalk of $AX = 45$ dB. The simulated AWG insertion loss, *IL* reached 6 dB where 4 dB is attributed to non-uniformity *ILU*.

To spectrally characterize the AWG with the co-integrated photodiodes, we conducted a wavelength scan (see Fig. 3a) with a tunable laser [53] from 800 nm to 900 nm. We simultaneously recorded the digitized values of the photodiode-signal from 511 channels for each wavelengths. One AWG channel is not coupled to a photodiode for testing purposes.

PIC design and fabrication

The chip was fabricated using a semiconductor-industry compatible 200 mm CMOS line at ams OSRAM, resulting in over 40 chips per wafer. The lower stack layers are equipped

with optoelectronic components such as photodiodes, pixel electronics, and ADCs. A $0.35\,\mu$m high voltage CMOS process was used for the electronics. In a wafer-scale back-end process, the waveguide layer stack is added, comprising of a 160 nm silicon nitride (SiN) waveguide core layer separated from the photodiodes by a $7\,\mu$m silicon-dioxide (SiO$_2$) layer, the top layer is $2\,\mu$m thick SiO$_2$. The waveguide core layer was deposited with a low-temperature PECVD (plasma-enhanced chemical vapor deposition). Lithographic structuring was carried out using deep-UV with a minimum possible feature size of 150 nm.

We designed the layout of the optical components with an in-house MATLAB (2007) program in combination with KLayout [54] In our simulations, we incorporated Beam-PROP (RSoft) and Lumerical FDTD (Finite Difference Time Domain). FDTD was used for the final optimization because it is capable of providing numerically correct results for Maxwell's equations. The waveguide-to-photodiode coupling structure includes a combination of two tapers and an aperiodic grating. For the first taper, we designed an inverted, mode-expanding taper that has a tip width of 800 nm increasing sinousiodally to $5\,\mu$m. This taper blends directly into the second taper (grating taper) that again sinusoidally decreases its width from $4.2\,\mu$m to 220 nm (at the 8th period of the grating). The taper tip width of 200 nm sets the minimum feature size of the structure. The grating's bar-to-period ratio (duty cycle) decreases as the distance from the input waveguide increases and the bar width reduces. It has a starting period of $3.75\,\mu$m and an ending period of $4.6\,\mu$m. The duty cycle of the grating at the light entry is 89%, and is reduced to 40%. The entire structure is enclosed by a $25\,\mu$m trench in the two SiO$_2$ layers consisting of a $2\,\mu$m top cladding and a $5\,\mu$m bottom cladding. The trench ends $3.5\,\mu$m above the photodiodes. A 100 nm thick aluminum layer is deposited and covers the entire trench. This aluminum metal cage surrounds the silicon nitride grating structure at a distance, where evanescent coupling from the dielectric waveguide is negligible. The waveguide-to-photodiode coupling structure was simulated with 3D FDTD. The photodiode was modelled by a silicon layer, with a monitor placed at the cladding/photodiode interface over the actual size of the photodiode. This monitor determined the optical power relative to the input power that would enter a photodiode taking into account interface reflections.

Loss measurements

The propagation losses were assessed using waveguide spirals of various lengths, all sharing the same waveguide design. The results revealed an average value of 1.56 dB/cm within the wavelength range of 850 nm − 900 nm.

All measurements were conducted using a tunable laser [53] and an Agilent 81619A mainframe equipped with two 81623B optical powerheads.

To determine the in-coupling losses, two measurements were performed on a test waveguide (200 nm width) integrated into the presented chip. Firstly, we measured the power between a polarization-maintaining (PM) fiber at the input and a single-mode (SM) fiber with the same mode field diameter (MFD) at the output of the test structure. Secondly, we used an external photodiode directly at the output instead of the SM-fiber to establish a lossless connection. By comparing these two measurements, we calculated the in-coupling losses from the SM-fiber without glycerol to the waveguide. Losses of

5.7 dB at a wavelength of 800 nm which decreases to 3.7 dB at a wavelength of 900 nm were measured.

The waveguide-to-photodiode coupling losses were determined on a test structure where the photodiode current could be measured. Measurements of the current were taken on two different PICs. One PIC had no waveguide layer stack, and the photodiode could be directly illuminated by a focuser. We obtained currents for different optical power and wavelengths. With these measurements we could establish a correlation between optical powers and the measured current, while accounting for losses from the focuser. For the second PIC, that had the waveguide layer stack, light was coupled into the waveguide leading to the same test structure using an SM-fiber (without glycerol) and the current was measured. Taking the in-coupling losses and propagation losses into account, we calculated the coupling losses (transmission efficiency) from the waveguide to the photodiode, see Fig. 3c.

OCT setup and image acquisition

The optical setup is depicted in Fig. 4a. We assembled a fiber-based SD-OCT system, replacing the spectrometer with the presented chip. Our light source is a superluminescence diode (SLD) (Thorlabs SLD880S-A25) with a central wavelength of 880 nm and a bandwidth of 40 nm, accompanied by an isolator (Thorlabs IO-F-SLD100-840). The light from the SLD (around 7 mW after the isolator) is split into a reference and sample arm by a 60/40% splitter (Gould). Both arms pass through polarization controllers and in both reflective collimators (Thorlabs RC04APC-P01) are used. An achromatic lens (AC254-050-B) is used to focus the light on the sample. The back-reflected light from the sample and reference arm couples into the chip through a bare fiber with a drop of glycerol to facilitate index matching. The AWG co-integrated with photodiodes captures interference between the two arms across the entire wavelength spectrum. The integrated ADCs directly convert this signal on the chip. This acquired data is recorded using a frame grabber (Xcelera-CL-PX4-1) with a custom camera file (Teledyne Dalsa CamExpert). The time it takes to acquire an image is adjustable. It can be modified by the integration time via an external signal generator (exposure control). The integration time of the photodiodes is also the A-scan rate. An A-scan is the depth profile of a single scanning position. By scanning over the sample many adjacent A-scans are acquired. With scanning in only one direction 2D images are generated, called B-scans, and 2-axis scanning produces 3D volumes. The B-scan rate (number of A-scans per B-scan) is configured within the camera file. To control both axes of the scan mirrors a DAQ card (NI PCIe-6351) delivers two analogue voltage signals. For the fast axis, a saw-tooth shaped signal with smoothed edges is utilized to acquire a B-scan. Data is recorded only during the upwards path of the saw-tooth, a process controlled by counting the A-scan triggers received directly from the PCB. The voltage signal for the slow axis of the scan mirrors is a simple step function. Synchronization of acquisition and the galvanometric scan mirrors is achieved through the A-scan trigger (Line Valid) directly from the PCB to the external trigger input of the frame grabber and the DAQ card for the galvo control. Acquisition and data processing are performed by using MATLAB (R2020b, R2022b). For all the measurements, a squared clock signal of 28 MHz with a 50% duty cycle and a squared signal

for the integration time with 55 kHz and a 90% duty cycle are chosen. To maintain a constant temperature of the chip during the OCT measurements, a thermoelectric cooler (TEC) is positioned underneath the PCB.

Standard post-processing steps are carried out to reconstruct the tomograms from the acquired data. Firstly, the data is sorted according to the camera link protocol using a lookup table. Additionally, for each measurement the signal exclusively from the reference arm is acquired by blocking the sample arm. This background signal is subsequently subtracted from the interference signal to mitigate fixed pattern noise. Next, the spectrum is resampled to get equally spaced wavenumbers from equally spaced wavelengths. The assignment of each pixel to the corresponding wavelength is extracted from the wavelength scan, as illustrated in Fig. 3b. Following this, a Hanning window is applied to the spectrum, which is then Fourier-transformed to generate the structural depth information of the sample, which is called an A-scan. Before averaging the tomograms of the in vivo skin, a B-scan registration [55] is performed to correct for motion. In the case of zebrafish larvae tomograms, this step is unnecessary as the larvae were anaesthetized prior to imaging. For the reconstruction of OCTA images, five B-scans are acquired on the same position. Following the same post-processing steps described earlier, Gaussian blurring (sigma equals two) is applied. Subsequently, the speckle variance, as described in [56, 57], is calculated across the repeated tomograms retaining intensity signals that exhibit changes over time, such as those from blood vessels.

Characterization of OCT system

To determine the characteristic parameters of the OCT system, a mirror is used as the sample. Sensitivity was measured with an additional ND-filter in the sample arm, resulting in a double path attenuation of 29 dB. Sensitivity is calculated by adding the attenuation to the logarithmic, squared ratio of the amplitude to the standard deviation of the noise. The axial resolution is given by the full width at half maximum (FWHM) of the point spread function. To measure the signal roll-off, the reference arm is adjusted to capture interference fringes throughout the entire imaging depth range. Lateral resolution was assessed using an USAF resolution target (Thorlabs R3L3S1P). Specifically, at the group 6 element 4 the lines can still be resolved by a 60% difference between the maxima and minima of the signal from the three lines of this element on the resolution target (see Fig. 4b).

To quantify the image quality of in vivo skin tomograms (Fig. 6), we calculated the image signal-to-noise ratio (SNR) and contrast-to-noise ratio (CNR) for increasing number of averages, ranging from averaging over two up to a hundred tomograms, see Fig. 8. For this purpose, we segmented the region of interest by thresholding the image histogram to create a mask for the finger. The region outside this mask is defined as background. The SNR is then calculated by the ratio of the maximum of the signal to the standard deviation of the noise (background). The CNR is calculated by taking the mean of the signal region, $\bar{S}$, and subtracting the mean of the noise region, $\bar{N}$, and then dividing this by the standard deviation of the noise, σ_N (see Eq. 1). We calculated the relative change of SNR and CNR with increasing number of averages in relation to SNR and CNR without any averaging.
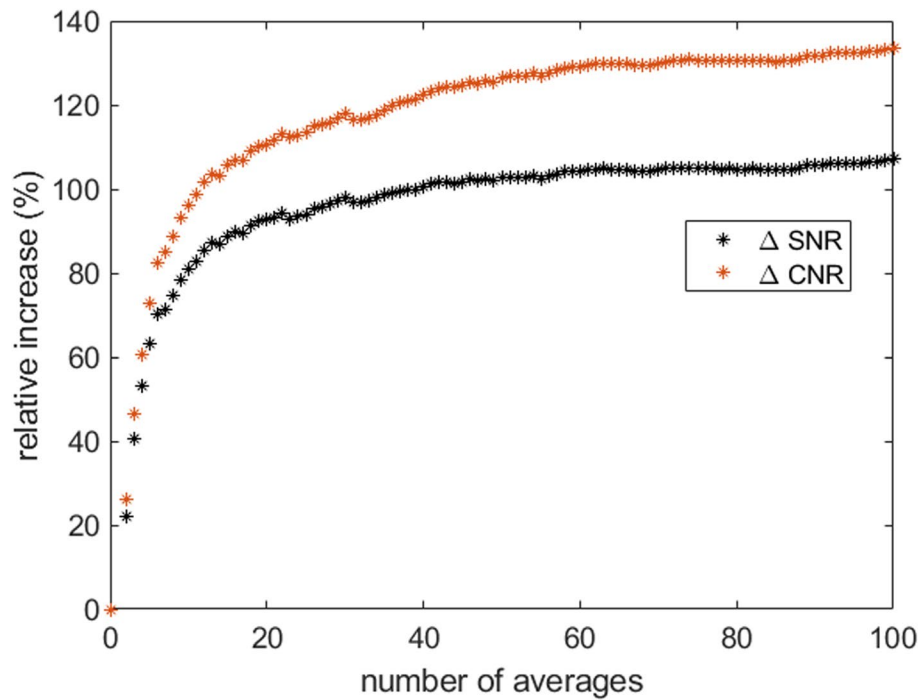
Fig. 8 Relative increase of SNR and CNR with the number of averages. The black curve demonstrates the relative increase in SNR with an increasing number of averages (2-100 averages) compared to no averaging. The red curve demonstrates the same for CNR. Averaging over a hundred tomograms leads to an increase of 107% in image SNR and 134% in image CNR

$$CNR = \frac{\bar{S} - \bar{N}}{\sigma_N} \qquad (1)$$

Simulation of signal roll-off

The signal roll-off was simulated using the device's spectral responses measured at each photodiode (shown in Fig. 3a), a modeled source spectrum having a Gaussian shape (FWHM = 30 nm) and modeled recorded signals with modulation frequencies in the range of one cycle per spectral sampling range up to the Nyquist limit (corresponding to the integer division of the number of photodiodes by 2). The recorded signals were modeled as area-normalized overlap integrals of each channel of the "ideal" interferometric signals with the respective measured spectral responses, thus representing the spectra convoluted by the spectral responses for each modulation. To ensure linear sampling in k-space, a k-mapping procedure was applied to the reconstructed interference signals. The signal roll-off was then computed from the signal peak heights after discrete Fourier transform (DFT) of the resultant interference signals and plotted over the calculated depth range. In addition, roll-off curves corresponding to the device's averaged spectral response and the device's best-performing 10 percent of AWG channels were calculated and plotted. The roll-off curve corresponding to the device's averaged spectral response was calculated based on the

convolution theorem. The reconstructed signal can be seen as convolution between the spectral responses with the "ideal" interference pattern. Thus, the Fourier transform of the spectral response defines the signal decay with depth yielding the envelope of the signal roll-off. The roll-off using only spectral responses measured at all photodiodes (without taking the source spectrum and recorded signal into account) is therefore calculated as follows: first, the DFT operation was applied to each spectral response, and then the absolute values of the resultants were averaged over the number of channels.

Fish preparation

Zebrafish (Danio rerio) with reduced pigmentation (Mitfab$^{692/b692/ednrb1b140/b140}$) were maintained according to standard protocols [58] with approval of the Austrian Bundesministerium fuer Wissenschaft und Forschung (GZ BMWF-66.008/0009-WF/II/3b/2014). Prior to imaging, the fish were anaesthetized in a 1% tricaine solution and then embedded in 1% Pythagel (Sigma Aldrich P8169-250G) in a glass-bottom petridish. In between measurements the larvae were kept in E3 medium (5 mM NaCl, 0.17 mM KCl, 0.33 mM CaCl2, 0.33 mM MgSO4) at 28°C.

Abbreviations

ADC	Analogue-to-digital converters
AWG	Arrayed waveguide grating
AX	Adjacent channel crosstalk
CCD	Charged-coupled device
CMOS	Complementary metal-oxide-semiconductor
CNR	Contrast-to-noise ratio
FDTD	Finite-difference time-domain
FPGA	Field programmable gate array
FWHM	Full width at half maximum
IL	Insertion loss
ILU	Insertion loss uniformity
OCT	Optical coherence tomography
OCTA	Optical coherence tomography angiography
PCB	Printed circuit board
PIC	Photonic integrated circuit
SD-OCT	Spectral domain optical coherence tomography
SLD	Superluminescent diode
SNR	Signal-to-noise ratio
TEC	Thermoelectric cooler

Supplementary Information

The online version contains supplementary material available at https://doi.org/10.1186/s43074-024-00150-7.

> Additional file 1. Rotating in vivo OCT volume of a zebrafish larva aged 4.5 days post fertilization (five times averaged). White scale bars correspond to 0.5 millimeters.

Authors' contributions

WD, RH, RL and PM conceived the general idea of the work. HZ, MV, PC, EB, AA and QN developed the electronics. JK, PC and MS fabricated the integrated spectrometer. DS, RH and PM designed the AWG and the coupling structure. ME, SN, AMN, ER, PM, QN and AA performed tests and characterization measurements of the chip. YM and RL did the roll-off simulations. AA carried out the OCT measurements. AA and QN developed the acquisition and postprocessing software. AA, QN and EB developed the camera file. NS and RAK provided the zebrafish larva and expertise in handling them. AA, PM, DS, RH, YM, RL and WD wrote the manuscript and all authors contributed to the manuscript.

Availability of data and materials
All relevant data supporting the study are available under https://osf.io/6z94g/?view_only=b1d2e74f9af1454687fe3b235d2326de.

Code availability
All relevant codes supporting the study are available from the corresponding author upon reasonable request.

Declarations

Ethics approval and consent to participate
For the skin tomograms, the study protocol and informed consent were reviewed and approved by the Ethics Committee of the Medical University of Vienna with protocol number EK-1246/2013. Prior to participation, all participants provided written informed consent. The research adhered to the principles of good clinical practice and was performed in accordance with the Declaration of Helsinki.

Consent for publication
All authors have given their consent for the publication of this paper.

Competing interests
The authors declare no competing interests.

References

1. Sancho-Durá J, Zinoviev K, Lloret-Soler J, Rubio-Guviernau JL, Margallo-Balbás E, Drexler W. Handheld multi-modal imaging for point-of-care skin diagnosis based on akinetic integrated optics optical coherence tomography. J Biophoton. 2018;11(10):e201800193. https://doi.org/10.1002/jbio.201800193.
2. Xiang C, Jin W, Bowers JE. Silicon nitride passive and active photonic integrated circuits: trends and prospects. Photon Res. 2022;10(6):A82. https://doi.org/10.1364/prj.452936.
3. Drexler W, Fujimoto JG. Optical Coherence Tomography. Switzerland: Springer International Publishing; 2015. https://doi.org/10.1007/978-3-319-06419-2.
4. Sattler E, Kästle R, Welzel J. Optical coherence tomography in dermatology. J Biomed Opt. 2013;18(6):061224. https://doi.org/10.1117/1.jbo.18.6.061224.
5. Welzel J, Noack J, Lankenau E, Engelhardt R. Optical Coherence Tomography in Dermatology. In: Handbook of Optical Coherence Tomography. Luebeck: CRC Press; 2001. pp. 539–61. https://doi.org/10.1201/b14024-21.
6. Vakoc BJ, Fukumura D, Jain RK, Bouma BE. Cancer imaging by optical coherence tomography: preclinical progress and clinical potential. Nat Rev Cancer. 2012;12(5):363–8. https://doi.org/10.1038/nrc3235.
7. Photiou C, Kassinopoulos M, Pitris C. Extracting Morphological and Sub-Resolution Features from Optical Coherence Tomography Images, a Review with Applications in Cancer Diagnosis. Photonics. 2023;10(1):51. https://doi.org/10.3390/photonics10010051.
8. Tsai TH, Fujimoto J, Mashimo H. Endoscopic Optical Coherence Tomography for Clinical Gastroenterology. Diagnostics. 2014;4(2):57–93. https://doi.org/10.3390/diagnostics4020057.
9. Agneter A, Rank EA, Schmoll T, Leitgeb RA, Drexler W. Miniaturizing optical coherence tomography. Transl Biophotonics. 2022;4(1-2). https://doi.org/10.1002/tbio.202100007.
10. Song G, Jelly ET, Chu KK, Kendall WY, Wax A. A review of low-cost and portable optical coherence tomography. Prog Biomed Eng. 2021;3(3):032002. https://doi.org/10.1088/2516-1091/abfeb7.
11. Yurtsever G, Považay B, Alex A, Zabihian B, Drexler W, Baets R. Photonic integrated Mach-Zehnder interferometer with an on-chip reference arm for optical coherence tomography. Biomed Optic Express. 2014;5(4):1050. https://doi.org/10.1364/boe.5.001050.
12. Ji X, Yao X, Gan Y, Mohanty A, Tadayon MA, Hendon CP, et al. On-chip tunable photonic delay line. APL Photon. 2019;4(9):090803. https://doi.org/10.1063/1.5111164.
13. Akca BI, Worhoff K, de Ridder RM, Nguyen VD, Kalkman J, Ismail N, et al. Toward Spectral-Domain Optical Coherence Tomography on a Chip. IEEE J Sel Top Quantum Electron. 2012;18(3):1223–33. https://doi.org/10.1109/jstqe.2011.2171674.
14. Akca BI, Považay B, Alex A, Wörhoff K, de Ridder RM, Drexler W, et al. Miniature spectrometer and beam splitter for an optical coherence tomography on a silicon chip. Opt Express. 2013;21(14):16648. https://doi.org/10.1364/oe.21.016648.
15. Ruis RM, Leinse A, Dekker R, Heideman RG, van Leeuwen TG, Faber DJ. Decreasing the Size of a Spectral Domain Optical Coherence Tomography System With Cascaded Arrayed Waveguide Gratings in a Photonic Integrated Circuit. IEEE J Sel Top Quantum Electron. 2019;25(1):1–9. https://doi.org/10.1109/jstqe.2018.2874074.
16. Smit MK. New focusing and dispersive planar component based on an optical phased array. Electron Lett. 1988;24(7):385. https://doi.org/10.1049/el:19880260.

17. Takahashi H, Suzuki S, Kato K, Nishi I. Arrayed-waveguide grating for wavelength division multi/demultiplexer with nanometre resolution. Electron Lett. 1990;26(2):87. https://doi.org/10.1049/el:19900058.

18. Smit MK, Dam CV. PHASAR-based WDM-devices: Principles, design and applications. IEEE J Sel Top Quantum Electron. 1996;2(2):236–50. https://doi.org/10.1109/2944.577370.

19. Seyringer D. Arrayed Waveguide Gratings. Spotlight. SPIE; 2016. https://doi.org/10.1117/3.2242852.

20. Seyringer D, Schmid P, Bielik M, Uherek F, Chovan J, Kuzma A. Design, simulation, evaluation, and technological verification of arrayed waveguide gratings. Opt Eng. 2014;53(7):071803. https://doi.org/10.1117/1.oe.53.7.071803.

21. Seyringer D, Hodzic E. Calculation of accurate channel spacing of an AWG optical demultiplexer applying proportional method. In: Fédéli JM, editor. SPIE Proceedings. 9520, Integrated Photonics: Materials, Devices, and Applications III, 95200T. SPIE; 2015. https://doi.org/10.1117/12.2178271.

22. Rank EA, Sentosa R, Harper DJ, Salas M, Gaugutz A, Seyringer D, et al. Toward optical coherence tomography on a chip: in vivo three-dimensional human retinal imaging using photonic integrated circuit-based arrayed waveguide gratings. Light Sci Appl. 2021;10(1). https://doi.org/10.1038/s41377-020-00450-0.

23. Richter A, Polatynski A, Mingaleev S, Sokolov E, de Felipe D, Conradi H, et al. Virtual prototyping of complex photonic components and integrated circuits for polymer-based integration platform. In: Lee EH, He S, editors. Smart Photonic and Optoelectronic Integrated Circuits XX. San Francisco: SPIE; 2018. https://doi.org/10.1117/12.2290436.

24. Nathan M. Microlens reflector for out-of-plane optical coupling of a waveguide to a buried silicon photodiode. Appl Phys Lett. 2004;85(14):2688–90. https://doi.org/10.1063/1.1803617.

25. Masini G, Sahni S, Capellini G, Witzens J, Gunn C. High-Speed Near Infrared Optical Receivers Based on Ge Waveguide Photodetectors Integrated in a CMOS Process. Adv Opt Technol. 2008;2008:1–5. https://doi.org/10.1155/2008/196572.

26. Byrd MJ, Timurdogan E, Su Z, Poulton CV, Fahrenkopf NM, Leake G, et al. Mode-evolution-based coupler for high saturation power Ge-on-Si photodetectors. Opt Lett. 2017;42(4):851. https://doi.org/10.1364/ol.42.000851.

27. Bernard M, Gemma L, Brunelli D, Paternoster G, Ghulinyan M. Coupling of Photonic Waveguides to Integrated Detectors Using 3D Inverse Tapering. J Lightwave Technol. 2022;40(18):6201–6. https://doi.org/10.1109/jlt.2022.3190041.

28. Wen P, Tiwari P, Mauthe S, Schmid H, Sousa M, Scherrer M, et al. Waveguide coupled III-V photodiodes monolithically integrated on Si. Nat Commun. 2022;13(1). https://doi.org/10.1038/s41467-022-28502-6.

29. Xue Y, Han Y, Wang Y, Li J, Wang J, Zhang Z, et al. High-speed and low dark current silicon-waveguide-coupled III-V photodetectors selectively grown on SOI. Optica. 2022;9(11):1219. https://doi.org/10.1364/optica.468129.

30. Roelkens G, Brouckaert J, Taillaert D, Dumon P, Bogaerts W, Thourhout DV, et al. Integration of InP/InGaAsP photodetectors onto silicon-on-insulator waveguide circuits. Opt Express. 2005;13(25):10102. https://doi.org/10.1364/opex.13.010102.

31. De Vita C, Toso F, Pruiti NG, Klitis C, Ferrari G, Sorel M, et al. Amorphous-silicon visible-light detector integrated on silicon nitride waveguides. Opt Lett. 2022;47(10):2598. https://doi.org/10.1364/ol.455458.

32. D'Agostino D, Desbordes T, Broeke R, Boerkamp M, Mink J, Ambrosius HPMM, et al. A monolithically integrated AWG based wavelength interrogator with 180 nm working range and pm resolution. In: Advanced Photonics for Communications. IPRSN. OSA; 2014. https://doi.org/10.1364/iprsn.2014.im2a.4.

33. Zhang Z, Wang Y, Wang J, Yi D, Chan DWU, Yuan W, et al. Integrated scanning spectrometer with a tunable microring resonator and an arrayed waveguide grating. Photon Res. 2022;10(5):A74. https://doi.org/10.1364/prj.443039.

34. Hainberger R, Müllner P. PHOTONISCHE INTEGRIERTE SCHALTUNG, AT Patent, EP4033282A1;WO2022161965A1. EP4033282A1;WO2022161965A1. 2022. https://patents.google.com/patent/EP4033282A1.

35. Vlaskovic M, Zimmermann H, Meinhardt G, Kraft J, Sagmeister M, Schoegler J. PIN-photodiode based active pixel in 0.35 µm high-voltage CMOS for optical coherence tomography. In: 2019 42nd International Convention on Information and Communication Technology, Electronics and Microelectronics (MIPRO). Croatia: IEEE; 2019. https://doi.org/10.23919/mipro.2019.8757194.

36. Vlaskovic M, Zimmermann H, Meinhardt G, Kraft J. Image sensor for spectral-domain optical coherence tomography on a chip. Electron Lett. 2020;56(24):1306–9. https://doi.org/10.1049/el.2020.1898.

37. Lichtenegger A, Baumann B, Yasuno Y. Optical Coherence Tomography Is a Promising Tool for Zebrafish-Based Research–A Review. Bioengineering. 2022;10(1):5. https://doi.org/10.3390/bioengineering10010005.

38. Narumanchi S, Wang H, Perttunen S, Tikkanen I, Lakkisto P, Paavola J. Zebrafish Heart Failure Models. Front Cell Dev Biol. 2021;9. https://doi.org/10.3389/fcell.2021.662583.

39. Astell KR, Sieger D. Zebrafish In Vivo Models of Cancer and Metastasis. Cold Spring Harb Perspect Med. 2019;10(8):a037077. https://doi.org/10.1101/cshperspect.a037077.

40. Gamble JT, Elson DJ, Greenwood JA, Tanguay RL, Kolluri SK. The Zebrafish Xenograft Models for Investigating Cancer and Cancer Therapeutics. Biology. 2021;10(4):252. https://doi.org/10.3390/biology10040252.

41. Schuermann A, Helker CSM, Herzog W. Angiogenesis in zebrafish. Semin Cell Dev Biol. 2014;31:106–14. https://doi.org/10.1016/j.semcdb.2014.04.037.

42. Isogai S, Horiguchi M, Weinstein BM. The Vascular Anatomy of the Developing Zebrafish: An Atlas of Embryonic and Early Larval Development. Dev Biol. 2001;230(2):278–301. https://doi.org/10.1006/dbio.2000.9995.

43. Hegasy D. Illustration. www.hegasy.de. Accessed 8 Mar 2023.

44. Seyringer D, Müllner P, Eggeling M, Agneter A, Nguyen Q, Rank EA, et al. 512-channel SiN-based AWG-spectrometer for OCT on a chip. In: 2024 24th International Conference on Transparent Optical Networks (ICTON). vol. 123. Bari: IEEE; 2024. pp. 1–4. https://doi.org/10.1109/icton62926.2024.10647672.

45. Leitgeb RA, Michaely R, Lasser T, Sekhar SC. Complex ambiguity-free Fourier domain optical coherence tomography through transverse scanning. Opt Lett. 2007;32(23):3453. https://doi.org/10.1364/ol.32.003453.

46. Wojtkowski M, Kowalczyk A, Leitgeb R, Fercher AF. Full range complex spectral optical coherence tomography technique in eye imaging. Opt Lett. 2002;27(16):1415. https://doi.org/10.1364/ol.27.001415.

47. Rarbi F, Dzahini D, Gallin-Martel L, Bouvier J. A low cross-talk 3-channel analog multiplexer with a 12-bit 25-MS/s pipelined ADC. In: 2012 IEEE Nuclear Science Symposium and Medical Imaging Conference Record (NSS/MIC). Anaheim: IEEE; 2012. https://doi.org/10.1109/nssmic.2012.6551233.

48. Yoon C, Bauer A, Xu D, Dorrer C, Rolland JP. Absolute linear-in-k spectrometer designs enabled by freeform optics. Opt Express. 2019;27(24):34593. https://doi.org/10.1364/oe.27.034593.

49. Seyringer, D. Application of angular method to correct channel spacing between AWG demultiplexed channels. In Advanced Manufacturing, Electronics and Microsystems. TechConnect Briefs. TechConnect. 2016. pp. 267–71.

50. Hodzic E, Seyringer D, Uherek F, Chovan J, Kuzma A. Calculation of accurate channel spacing of an arrayed wave-guide grating optical multiplexer/demultiplexer applying position method. In: The Tenth International Conference on Advanced Semiconductor Devices and Microsystems. Smolenice: IEEE; 2014. https://doi.org/10.1109/asdam.2014.6998685.

51. Seyringer D. Arrayed waveguide gratings for telecom and spectroscopic applications. In: Integrated Optics Volume 2: Characterization, devices and applications. [online]. Institution of Engineering and Technology; 2020. pp. 295–336. https://doi.org/10.1049/pbcs077g_ch10.

52. PHASER tool from Optiwave. https://optiwave.com/resources/academia/wdm-phasar-download/. Accessed 2023.

53. SolSTis Ti:Sapphire laser, M Square, 1 Kelvin Campus, West of Scotland Science Park, Glasgow, United Kingdom. https://m2lasers.com. Accessed Apr 2023.

54. KLayout. https://www.klayout.de. Accessed 2023.

55. Guizar-Sicairos M, Thurman ST, Fienup JR. Efficient subpixel image registration algorithms. Opt Lett. 2008;33(2):156. https://doi.org/10.1364/ol.33.000156.

56. Mariampillai A, Standish BA, Moriyama EH, Khurana M, Munce NR, Leung MKK, et al. Speckle variance detection of microvasculature using swept-source optical coherence tomography. Opt Lett. 2008;33(13):1530. https://doi.org/10.1364/ol.33.001530.

57. Zhang A, Zhang Q, Chen CL, Wang RK. Methods and algorithms for optical coherence tomography-based angiography: a review and comparison. J Biomed Opt. 2015;20(10):100901. https://doi.org/10.1117/1.jbo.20.10.100901.

58. Westerfield M. The Zebrafish Book; A guide for the laboratory use of zebrafish (Danio rerio). 4th Edition. Eugene. 2007;1:1–3.

Publisher's Note